Finite-Element Analysis of Bulk-Acoustic-Wave Devices: A Review of Model Setup and Applications

Robert K. Thalhammer, *Member, IEEE*, and John D. Larson, III, *Life Fellow, IEEE*

***Abstract*— In this paper, the principles of finite-element modeling for the electroacoustic simulation of bulk-acoustic-wave devices will be summarized. We will outline the model setup including governing equations and boundary conditions, as well as its efficient computer implementation. Particular emphasis will be given to tailoring the model dimension to the specific requirements of the desired investigation. As 3-D simulations still require a major effort, it will be illustrated that various aspects of device physics and design can already be addressed by fast and efficient 2-D simulations. Multiple theoretical and experimental evidence will be presented to demonstrate the validity of the modeling concepts. Based on various examples, it will be sketched how to benefit from numerical simulations for understanding fundamental effects, designing devices for actual products, and exploring novel technologies.**

***Index Terms*— Bulk acoustic wave (BAW), film BAW resonator (FBAR), finite-element modeling (FEM), RF devices.**

I. Introduction

As THE gigahertz frequency range is very popular for wireless data transmission, the increasing demand makes this spectrum more and more crowded and raises the challenges for employed technologies. The front-end modules attached to the device antennas experience a tremendous trend toward higher levels of integration, where both the number and the diversity of components keep increasing. One of the key technologies for RF filters is based on devices using the piezoelectric effect [1], in particular the excitation of bulk acoustic waves (BAWs). Premium performance of the entire module requires a sophisticated optimization both at the system level to make all the components work together in the best way and for each building block such as the resonators. While the former typically constitutes an electromagnetic problem, optimizing BAW resonators couples different domains of physics, at least mechanical and electrical. Among the major design goals for the resonators are still the best possible Q-values and the purity of the main resonance.

Enabled by powerful computers and more and more efficient algorithms, numerical simulations based on finite-element modeling (FEM) get more and more important in every area of today's research and development activities. This paper summarizes the key steps for creating an appropriate and efficient model for BAW resonators and extends the previous overview reported in [2]. While a lot of work is done on the mathematical techniques and comprehensive publications are available in the literature, it is the purpose of this paper to take the user's perspective. That means we will focus on what needs to be done for setting up and implementing a tailored model as well as how to benefit from the simulation results.

Manuscript received December 24, 2015; accepted April 11, 2016. Date of publication April 20, 2016; date of current version October 1, 2016.

R. K. Thalhammer is with the Wireless Semiconductor Division, Avago Technologies GmbH, a Broadcom Ltd company, Munich 81737, Germany (e-mail: robert.thalhammer@broadcom.com).

J. D. Larson III is with Broadcom Ltd, San Jose, CA 95120 USA (e-mail: john.jarson@broadcom.com).

Digital Object Identifier 10.1109/TUFFC.2016.2555306

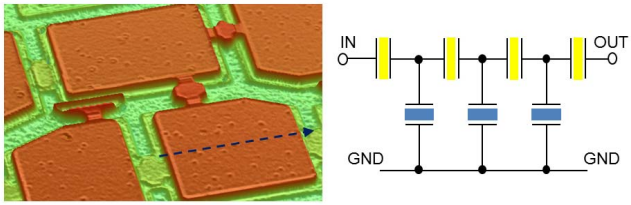

Fig. 1. Ladder-type filter based on BAW resonators. Left panel shows a partial image of a filter (orange areas are the resonators). It is based on a typical circuit comprising series resonators (yellow) and shunt resonators (blue) as sketched on the right.

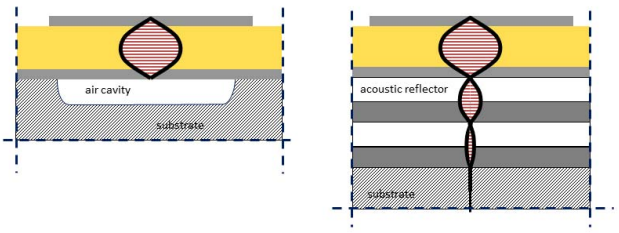

Fig. 2. Cross section through a BAW resonator as indicated by the arrow in Fig. 1, left panel. Each resonator can be either a membrane device (left) where reflection off the bottom surface is accomplished by an air cavity or an SMR with an acoustic mirror (right).

II. Model Setup

RF filters are typical applications of BAW resonators, where multiple of them are connected in an electrical circuit, such as the ladder type filter shown in Fig. 1. Each resonator comprises a piezoelectric layer between two electrodes. The electric field excites a vertically propagating wave that gets reflected off the top surface. Reflection at the bottom is either accomplished by an air cavity under the resonator or by an acoustic reflector comprising an alternating sequence of high- and low-impedance materials (Fig. 2).

This section summarizes the steps for the model setup, i.e., choosing the physical system of governing equations and their respective boundary conditions, selecting an analysis type, as well as numerical implementation and discretization.

The important aspect of tailoring the number of dimensions of the simulation domain is discussed in the next section.

A. Governing Equations and Boundary Conditions

In a BAW resonator, multiple physical domains interact with each other, at least mechanical (=acoustical) and electrical [3]. Optionally, also further physical domains could be added to the model, for example, the thermal domain.

1) System of Equations: Choosing the system of equations is straightforward and comprehensively discussed elsewhere [4]. The minimum set comprises the Maxwell equation reflecting the electric domain and Newton's equation of motion for the mechanical domain

$$\text{div}\, \boldsymbol{D} = 0 \tag{1}$$

$$\nabla \cdot \boldsymbol{T} - \rho \partial^2 \boldsymbol{u}/\partial t^2 = 0. \tag{2}$$

The symbols $\boldsymbol{D}$, $\boldsymbol{T}$, ρ, and $\boldsymbol{u}$ represent the dielectric displacement, mechanical stress, mass density, and mechanical displacement, respectively. The two domains are coupled by the piezoelectric effect, represented by the constitutive equations

$$\boldsymbol{T} = c_E \boldsymbol{S} - e\boldsymbol{E} \tag{3}$$

$$\boldsymbol{D} = \varepsilon_S \boldsymbol{E} + e\boldsymbol{S}. \tag{4}$$

Here, they are expressed in terms of the mechanical strain $\boldsymbol{S}$ and the electric field $\boldsymbol{E}$ with the material parameters stiffness c_E at constant electric field, dielectric coefficient ε_S at constant strain, and piezoelectric coefficient e. Representations using a different basis like $\boldsymbol{S}$ and $\boldsymbol{D}$, for example, are also possible.

2) Mechanical Boundary Conditions/Absorbing Boundaries: The mechanical boundary conditions in the vertical direction are a vanishing normal stress, representing free surfaces at the bottom and top of the resonator. While this is the best choice for a membrane device, solidly mounted resonators (SMRs) can be modeled more efficiently by not including the substrate and putting an absorbing boundary, as discussed in the following, at the bottom surface of the acoustic mirror.

Laterally, BAW resonators are typically embedded in a larger system, such as a filter, which is too complex to be handled by FEM simulations. Instead, the simulation domain has to be laterally truncated to the actual resonator and its near vicinity. The best choice for the boundary conditions at these artificial interfaces is absorbing boundaries. It corresponds to the view that any wave leaking out of the resonator will not feedback or create any impact on a different resonator.

There is no simple solution to realize an absorbing boundary. The most common technique is the so-called perfectly matched layer (PML), an artificial extension of the simulation domain with a complex transformation of the normal spatial direction. The fundamental problem is to get any type of wave absorbed in the same way, independent of polarization, angle of incidence, or propagation constant. As a simple example, replacing x by ix inside a PML will transform a propagating wave $\exp(ikx)$ to a damped wave $\exp(-kx)$. However, at the same time, it will transform an evanescent wave $\exp(-kx)$ to a propagating wave $\exp(-ikx)$.

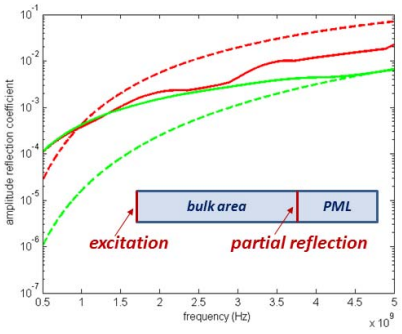

Fig. 3. Amplitude reflection coefficient for different types of PMLs under test, calculated by the test structure (inset). The method is described in the text. The colors refer to the two different PMLs, the solid lines represent reflection of longitudinal waves, and the dashed lines refer to shear waves.

That constitutes an artificial source of energy and may cause an S-parameter larger than 1. Hence, more sophisticated transformations are required. A lot of work is done on PMLs (see [4]–[11]) and multiple transformations have been proposed, for example the transformation [10]

$$x \to \tilde{x}(x) = x - i \int_{x\text{PML}}^{x} \sigma (\xi - x_{\text{PML}})^2 d\xi \tag{5}$$

where $\tilde{x}$ denotes the transformed coordinate inside the PML, xPML is the position of the interface to the PML, and σ represents a damping parameter. In general, it does not matter what the displacement profile inside the PML looks like—the relevant aspect for realizing an absorbing boundary is that the reflection off the interface to the PML is as little as possible. An initial assessment can be gained by a simple 1-D test (see the inset of Fig. 3): a wave is excited at the left edge of a transmission line (bulk area) by setting the boundary condition to a prescribed displacement in the direction along the transmission line for launching a longitudinal wave (or perpendicular to create a shear wave). The right end of the transmission line is terminated by the PML under test. The boundary conditions at its right edge do not really matter; they can be set to a clamped edge. For any real PML, an incident wave is not perfectly absorbed, but partially reflected. Thus, we get a standing wave distribution along the transmission line, from which the maximum and minimum displacement amplitudes $u_{\max}$ and $u_{\min}$ are extracted. The magnitude of the PML's reflection coefficient is calculated by $R = (u_{\max} - u_{\min})/(u_{\max} + u_{\min})$. This frequency-dependent test is run separately for longitudinal and shear waves. Fig. 3 compares two different types of PMLs, the first one according to (5) with $\sigma = 25\ \mu\text{m}^{-2}$ [10] and the second one based on the transformation $x \to \tilde{x}(x) = x(1 - 9i)$. These two types of PMLs have been used for simulating a membrane resonator as shown in Fig. 8 with the layer stack described in Fig. 7. As it can be seen from Figs. 4 and 5, PML 1 produces a slightly larger circle of the main mode and more pronounced spurious modes, in particular beyond f_p. The mode at 1880 MHz shows an S-parameter even larger than 1—a senseless result for a passive device, indicating numerical artifacts caused by the PML. Note that also for $S(f) < 1$, potential problems could exist, but they are not obvious as long as the artificial

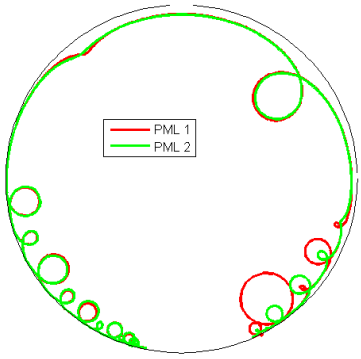

Fig. 4. Smith chart of a resonator terminated by the two different types of PMLs investigated in Fig. 3. The resonator is sketched in Fig. 8.

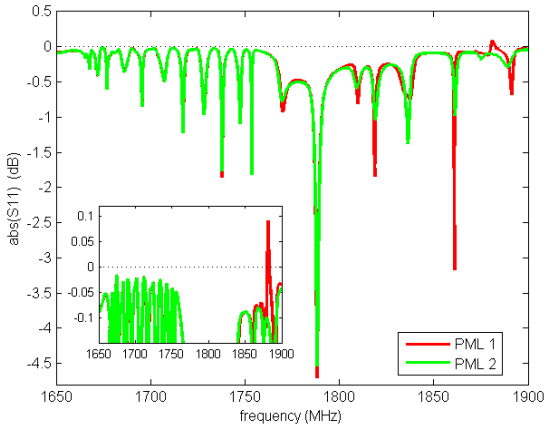

Fig. 5. Magnitude of the S_{11}-parameter plotted in Fig. 4. Inset: the same data with a zoomed-in view to the S_{11} values around 0 dB. As a resonator is a passive device, the values larger than 0 in the logarithmic scale are evidence of numerical artifacts.

gain by the PML is smaller than the total loss in the resonator. For the type of resonator in this example, PML 2 works better as already suggested by the lower reflection coefficient in Fig. 3. Note that the 1-D test does not cover the performance of PMLs terminating structures in 2-D or 3-D, but provides a quick initial assessment for tailoring the PML properly to the desired application.

3) FEM/BEM Methods: An alternative implementation of absorbing boundaries can be realized by the boundary element method (BEM). The BEM expands the unknown solution in terms of basis functions and the expansion coefficients are the computational variables [12], [13]. As it does not require a fine mesh, it is an efficient technique for covering a large simulation domain and the basis functions can be chosen to cover wave propagation in only one direction. Thus, BEM domains can be attached to the boundary of an FEM domain to form an absorbing boundary, for example, at the bottom surface of an acoustic mirror of an SMR [14], [15]. As this option is only available if the employed software can handle both FEM and BEM techniques and a comprehensive discussion of setting up BEM domains would be beyond the scope of this paper, the reader is referred to the literature for details.

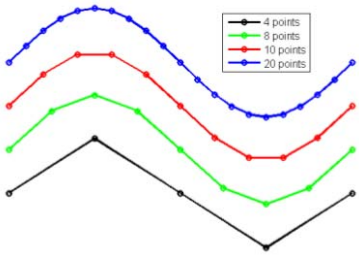

Fig. 6. Sine wave represented with different number of grid nodes per wavelength.

4) Electrical Boundary Conditions: As there is no normal current at the lateral boundary, a Neumann boundary condition (zero normal gradient of the potential) applies there. In the vertical direction, the most common choice for terminating the electrical simulation domain is defining the interfaces of the piezoelectric layer and the electrodes to be equipotential surfaces bound to the respective terminal voltages. In this case, the electrodes can be excluded from the simulation domain of the Maxwell equation. That reflects the view of infinite speed of light and perfectly conducting electrodes.

Including Ohm's law to cover electrode resistivity would be a rather straightforward extension of the system of equations. However, the decisive aspect for a meaningful model is the question of where to put the electric terminals in the simulation domain. Two-dimensional simulations can cover the center to edge variation of the electric potential across the resonator. However, the more interesting effects are the $x-y$ distribution of the current density and the potential inhomogeneity for a typically asymmetric position of the contact leads. For that purpose, the considerable effort of a 3-D model is required that has not been published yet. A 2-D FEM study with finite conductivity and a 3-D lumped element analysis of Ohmic losses is reported in [16] and [17].

B. Analysis Types

While time domain analysis is extremely inefficient for weakly damped systems, eigenmode analysis reveals which modes exist, but does not tell us by how much they are excited during actual operating conditions of a resonator. For extracting many desired figures of merit, e.g., Q-values, frequency domain analysis is the most preferred technique as it is able to cover properly the extent of electrical and acoustical losses and the amount of spurious mode excitation.

C. Numerical Implementation

After the analytical models to reflect the desired physical effects have been chosen, the user needs to decide on the mesh and the strategy for solving the discretized equations.

1) Discretization: The optimum mesh size is governed by two factors: the typical feature size of the geometry and the characteristic length of the physics of the device. The latter effect is related to the wavelength of the modes. As it is obvious from Fig. 6, a reasonable discretization width is about ten nodes per wavelength. Note that the decisive mode is the one with the smallest wavelength. Its value can be extracted from the dispersion diagram (see Fig. 7) calculated by the

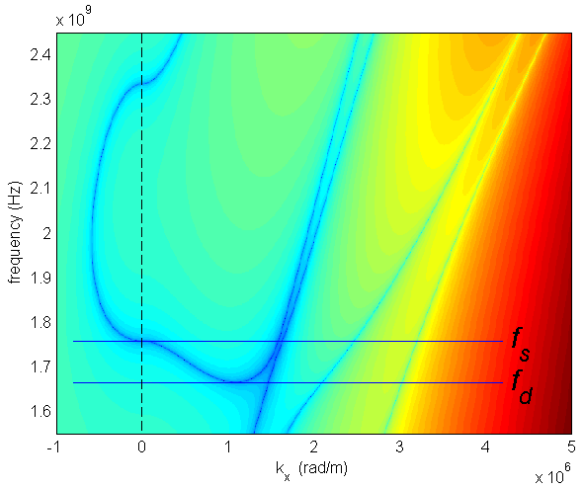

Fig. 7. Plate dispersion of a membrane resonator with a 500-nm Mo bottom electrode, a 1000-nm AlN piezo layer, and a 400-nm Mo top electrode, calculated by the matrix techniques [18]–[20]. The dark lines indicate the dispersion branches of the various modes. Propagating modes (real k_x-values) are plotted on the positive k_x-axis, evanescent modes (imaginary k_x-values) are plotted on the negative k_x-axis, and complex modes are not shown. The cutoff frequency is at $k_x = 0$ and is equal to the series resonance frequency f_s. The minimum frequency of the negative slope of the main dispersion branch is called f_d.

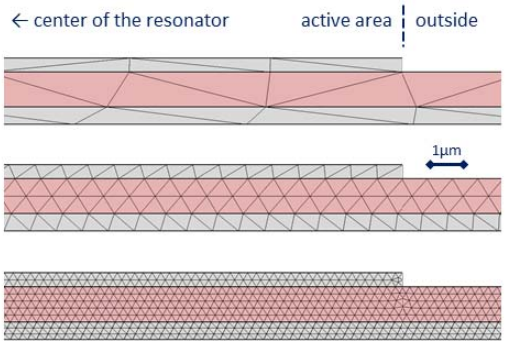

Fig. 8. Cross section through the edge of a membrane resonator comprising a piezoelectric AlN layer (red region) sandwiched by two Mo electrodes (gray region). The three images illustrate the discretization by differently fine meshes.

matrix techniques reported in [18]–[20]. In this example, propagating modes have k_x-values up to about 4 rad/μm, corresponding to a lateral wavelength of 1.6 μm. A grid size of about 200 nm should therefore not be exceeded. Verifying whether the chosen mesh is sufficient can be done by inspecting if the FEM results look smooth across the grid nodes and/or by rerunning the simulation with a finer mesh and double checking if the results are reproduced.

As an example, different meshes as shown in Fig. 8 have been used for 2-D simulations of a membrane resonator. Figs. 9 and 10 reveal that the medium mesh with quadrilateral elements of about 0.5 μm in size produces all modes qualitatively correctly, but differences to the results obtained with the fine mesh are obvious. These differences are smaller close to f_s, where the lateral wavelength of the main mode gets very large, and thus discretization is less critical.

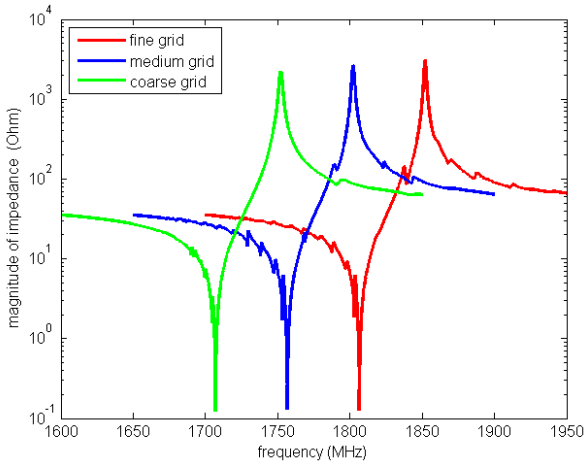

Fig. 9. Impedance characteristics for the different discretization widths sketched in Fig. 8. The traces have been shifted by 50 MHz to enable a clear distinction; the resonance frequencies are almost independent of discretization.

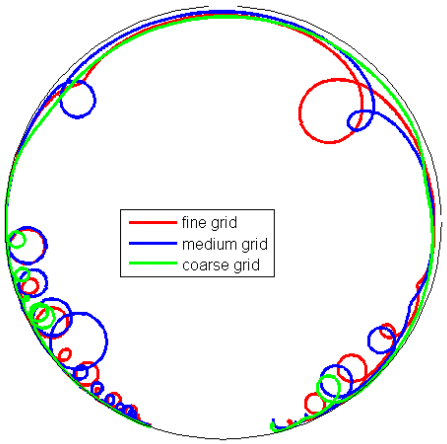

Fig. 10. Smith chart of the resonator response simulated with different meshes as shown in Fig. 8.

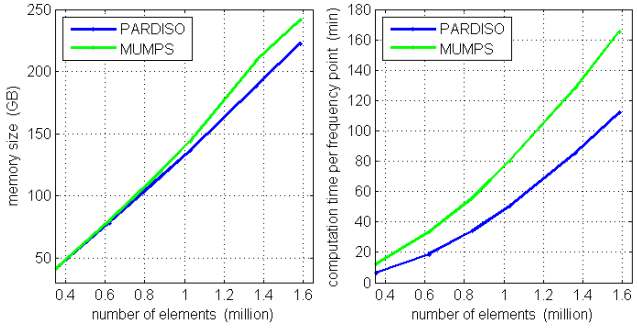

Fig. 11. Memory requirements (left) and computation time per frequency point (right) for 3-D simulations using different direct solvers.

2) Computational Aspects: For illustrating the ballpark of the number of required mesh elements, let us consider a resonator with an active area size of about 100 μm × 100 μm and a thickness of about 2 μm. Thus, meshing a 2-D cross section with a 200-nm grid size requires about 5000 elements, while a comparable mesh for the entire 3-D geometry needs about 2.5 million elements. Fig. 11 outlines the corresponding

TABLE I
EXAMPLES OF RESONATOR PROPERTIES COVERED BY DIFFERENT MODEL DIMENSIONS

Model Dimension	Effect / Resonator Property
1D	Resonance Frequencies, Reflectivity of acoustic mirrors
2D	Energy leakage at the edges, Optimum geometry of frames for spurious mode suppression and/or energy confinement
3D	Spurious mode reduction by apodization, Current distribution across electrodes with finite conductivity

memory requirements for 3-D. They are on the order of some 100 GB, which is feasible with modern computers. The actual problem is the computation time as a 3-D simulation typically takes a few hours per frequency point [see Fig. 11 (right)]. As a consequence, a frequency sweep with about 200 points would take several days to a few weeks, while a comparable analysis in 2-D is done in some minutes. These are principle ballparks, though a factor of around 2× to 5× can be accomplished using a more powerful computer and/or tuning the numerical solvers. For example, the comparison in Fig. 11 reveals that the licensed solver PARDISO [21], which is used in most of today's commercial FEM software packages, requires little less memory than the public domain solver MUMPS [22], but in particular, it is more efficient in terms of calculation time.

An alternative would be using iterative solvers, which consume significantly less memory and could be very fast. However, they require a sophisticated setup including appropriate preconditioners and might not converge at all for strongly coupled phenomena like electromechanical effects. For these kinds of problems, direct solvers are much more reliable.

III. TAILORING THE SPATIAL DIMENSION OF THE MODEL

As 3-D models require considerably larger computational efforts than 2-D models, a careful choice of the number of dimensions is essential for efficient simulations. It does not have to be 3-D, just because the devices are 3-D. The appropriate dimension is rather governed by the physics of the effect that we like to investigate (see Table I). For instance, the resonance frequencies in a sufficiently large resonator are already accurately predicted by a 1-D model. As will be shown in the following, edge termination by frames for energy confinement and/or spurious mode suppression is an example for effects that are well addressed by 2-D FEM. Still some effects require 3-D simulations, for example, apodization. This section illustrates which effects can be addressed by a limited number of model dimensions and provides experimental evidence for the validity of the concepts.

A. Figures of Merit

Whereas simulations for a particular device will naturally provide terminal characteristics, e.g., impedance versus frequency, we are typically interested in only a few properties, e.g., Q-value. While slightly different ways to extract these figures of merit are in place, a straight forward assessment of the device performance is obtained by averaging the magnitude of the S-parameter in a given frequency range

$$\langle S \rangle = (f_2 - f_1)^{-1} \int_{f1}^{f2} |S(f)| df. \tag{6}$$

Note that for a perfect resonator, $S(f) = 1$ at any frequency and thus $\langle S \rangle = 1$ for any interval $[f_1 f_2]$. Each definition according to (6) depends on the frequency interval $[f_1 f_2]$ and multiple of them can be selected. For example, choosing the frequency interval from f_d to f_s in a dispersion type II resonator will create a measure of the amount of spurious modes.

The major motivation for introducing quantities according to (6) is to get a stable evaluation of 2-D simulations. As they correspond to a structure with parallel edges, results are typically impacted by more pronounced spurious modes than there would be in a real device without parallel edges. For example, calculating the maximum device impedance R_p by $Z_{11}(f_p)$ will be distorted if there is a spurious mode close to f_p. A more reliable performance indicator is gained from (6) using an interval $[f_1, f_2]$ around f_p and calculating R_p by $Z_0(1+\langle S \rangle)/(1-\langle S \rangle)$. The 2-D results shown in the following are based on this definition.

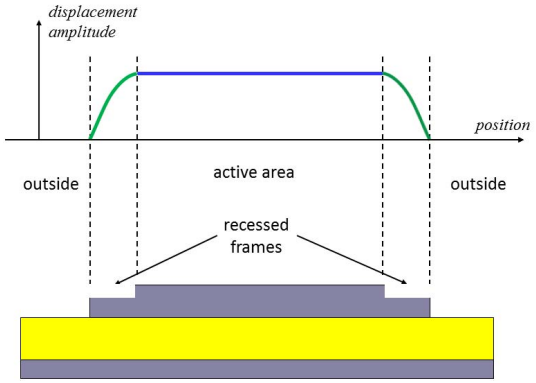

Fig. 12. Spurious mode suppression in a dispersion type II resonator: if we neglect the evanescent displacement profile outside the resonator, there is a node at the edge of the top electrode. The frame can be considered to transform this node to a crest at the interface of the frame and the active area, thus enabling the piston mode. For that purpose, the frame width needs to be quarter wave.

B. Spurious Mode Suppression by Recessed Frames

Spurious modes in a dispersion type II device can be suppressed by putting a recessed frame along its perimeter [23]. This is a concept that is well represented by 2-D simulations.

The theoretical displacement profile for the optimum configuration is sketched in Fig. 12: if the evanescent displacement distribution outside the resonator is neglected, the top electrode edge can be considered a quasi-node in the lateral direction. Transforming this node to a crest at the interface to the active area enables a uniform excitation (piston mode). As explained in [23], this configuration maximizes the coupling of the main mode and minimizes the coupling of any

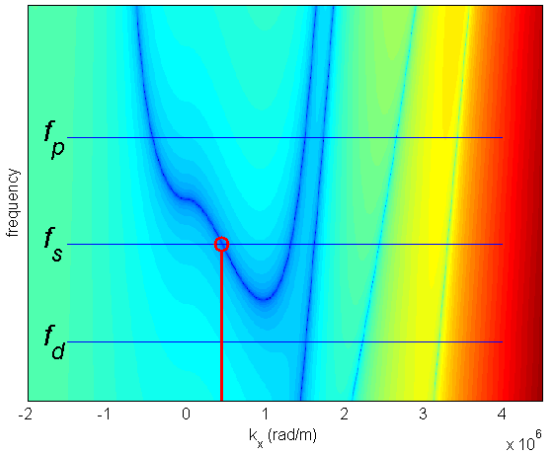

Fig. 13. Dispersion diagram of the layer stack in the recessed frame (color shading) calculated by the common matrix techniques [18]–[20]. Positive k_x-values refer to propagating modes and negative k_x-values represent evanescent modes. The solid lines correspond to the resonance frequencies of the active area. That means that at f_s, the k_x-value in the recessed frame is 0.45 rad/μm.

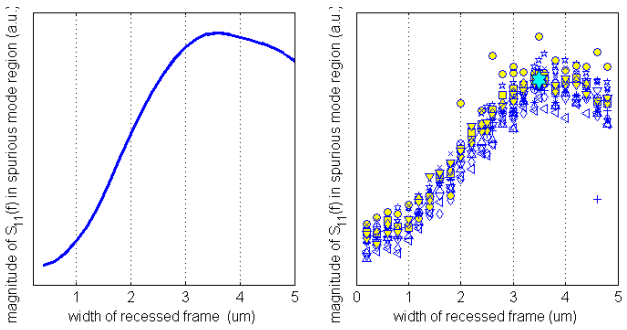

Fig. 14. Edge termination of a dispersion type II resonator by a recessed frame. The magnitude of $S_{11}(f)$ in the frequency interval from f_d to f_s has been used as a measure for spurious mode content. Left: 2-D simulation. Right: experimental result. The maximum is attained at 3.5 μm, which corresponds to the best spurious mode suppression.

other mode, thus suppressing the excitation of spurious modes. For performing the mentioned transformation, the optimum frame width has to be a quarter wave in the frame area at the cutoff frequency of the active area. $K_{x,\mathrm{opt}}$ can be seen from the dispersion diagram to be 0.45 rad/μm (see Fig. 13), so the optimum frame width is about 3.2 μm.

Two-dimensional simulations predict that the recessed frame works best if it is about 3.5–4 μm wide [see Fig. 14 (left)]. This simulation result is confirmed by both the theory as explained above and the experimental results shown in Fig. 14 (right). Whereas the attained level of spurious mode suppression is more difficult to predict, the ballpark for the optimum geometry is very accurately reflected by the simulation.

C. Energy Confinement by Raised Frames

In a dispersion type II resonator, raised frames improve the confinement of the acoustical energy in the active area. As a consequence, the maximum device impedance R_p attained at f_p increases. The periodicity of R_p on raised frame width is found to be governed by the k_x-value of the positively sloped

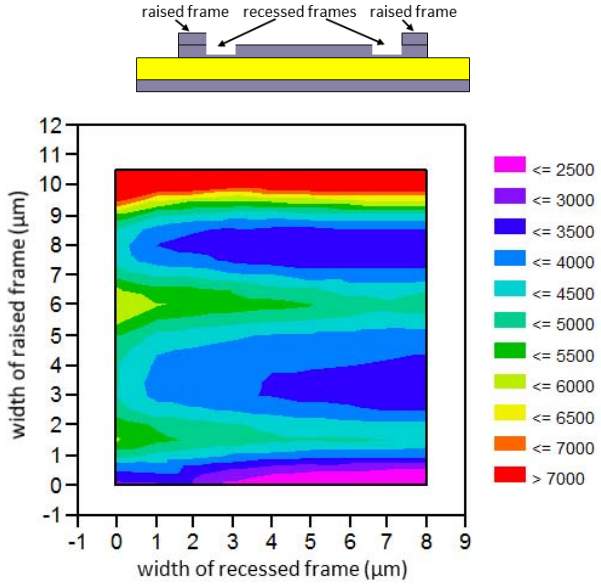

Fig. 15. Experimental results for R_p (maximum resonator impedance at f_p) versus the width of two frames, a recessed frame, and a raised frame (top) (figure courtesy of Alexandre Shirakawa).

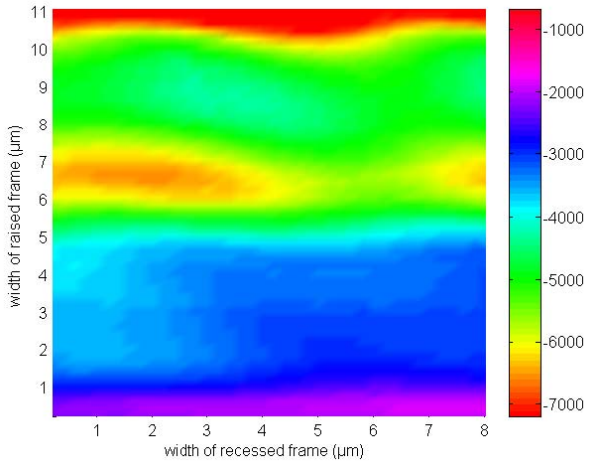

Fig. 16. Two-dimensional simulation results for R_p versus the width of two frames, a recessed frame and a raised frame.

section of the main dispersion branch. At the same time, the impact of the recessed frames on R_p is fairly weak [24]. Figs. 15 and 16 compare the measurement and simulation results for R_p dependence on the widths of recessed and raised frames. The characteristic features are accurately reproduced by the 2-D simulation, i.e., the weak dependence of R_p on the width of the recessed frame and the trend that narrower frames work better, as well as the ballparks for optimum widths of the raised frames with a first weak peak around 1.5–2 μm, a stronger one at about 6 μm, and a pronounced optimum beyond 10 μm. Also in this case, the overall level for the target figure of merit (here R_p) is reflected less accurately, but the ballparks of where to find the optimum device geometry are predicted reliably.

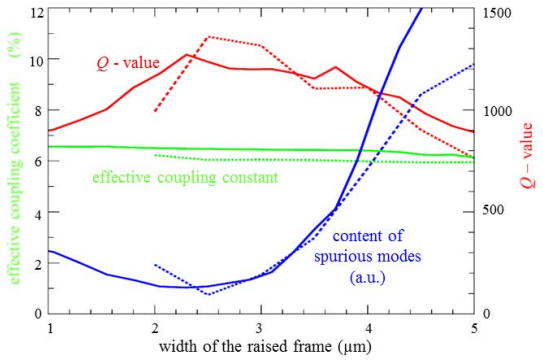

Fig. 17. Results of 2-D simulations (dashed lines) for some key characteristics of a dispersion type I resonator are compared with experimental results (solid lines).

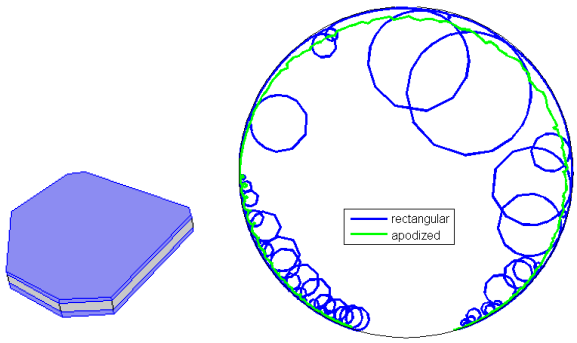

Fig. 18. Smith chart for an apodized resonator and a rectangular resonator. To exaggerate the effect of spurious modes, the entire resonator has been truncated to the same shape as the patterned top electrode, as shown for the apodized structure in the inset on the left. The layer stack is listed in Fig. 7; thicknesses have been scaled in the schematic.

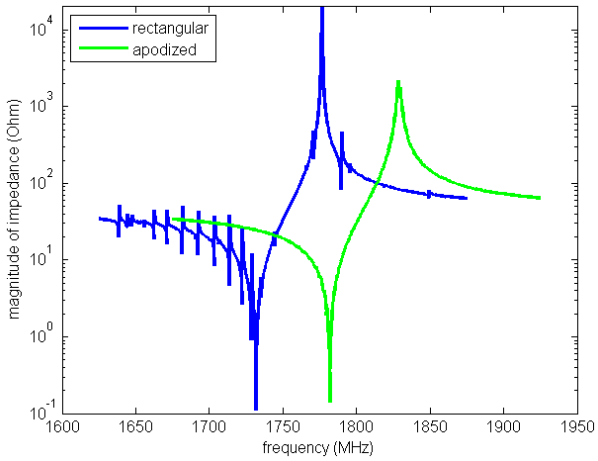

Fig. 19. Impedance characteristics of an apodized resonator and a rectangular resonator as shown in Fig. 18. Frequencies have been shifted by an offset of 50 MHz to enable a clear distinction.

D. Dispersion Type I Resonators

Resonators with a positive slope of the main dispersion branch (type I) require a raised frame for spurious mode suppression. A corresponding analysis is reported in [25]. For the key properties shown in Fig. 17, the results of the 2-D FEM are in excellent agreement with the experiments also for this type of device. Hence, we conclude that frame design is one of the examples, where 2-D models are valuable tools that reliably predict these desired features of the 3-D resonators.

E. Apodization

Another common technique to mitigate the impact of spurious modes in any type of resonator is apodization, i.e., designing the resonator area in the most possible irregular shape [26]. Thus, the length of a lateral closed path is increased and randomized, which significantly reduces the coupling of spurious modes. Besides, their random resonance frequencies result in a smoother electric resonator response. Combining this concept with the dispersion of the layer stack requires running simulations in 3-D.

The effect can be demonstrated in an extreme way by truncating all the layers to the shape of the top electrode (see Fig. 18). This anchorless resonator does not have lateral losses, and hence, any spurious mode has a very large Q-value. The simulation results for a rectangular resonator show the expected pronounced spurious modes, whereas the apodized resonator produces a much cleaner response, however, at the penalty of a lower average Q-value (see Figs. 18 and 19). This example demonstrates that apodization is a powerful technique to smooth the electric response, though many acoustic modes might still be excited in the interior of the resonator.

IV. Summary of Model Limitations and Accuracy

Several mathematical and physical factors limit the total accuracy of the FEM analysis: there is no issue with the precision of floating point operations, that is in the ballpark of 10^{-16}, and with the numerical accuracy, i.e., the residual error of solving the algebraic system of discretized equations. The latter is typically about 10^{-3} to 10^{-6} if the solver has converged properly, which is an important issue for nonlinear equations and/or iterative solvers. More attention needs to be paid to the discretization error, i.e., how well the continuous analytical solution is represented by the discrete set of algebraic function values on the finite grid. This error is about a few percent for proper meshes. Too coarse meshes can increase this error significantly or even change the solution qualitatively, e.g., if the solution comprised a propagating wave with a wavelength shorter than twice the grid size, it will not be covered at all or aliased to a different k-value. As shown previously, similar problems could arise from special implementation techniques to mimic configurations without a consistent mathematical representation, e.g., a frequency-dependent dielectric constant in a time domain analysis or absorbing boundaries in real space.

Typically, the greatest limitation is set by the physical effects included or not included in the model, these are:

1) The implications of the chosen set of equations, e.g., isothermal operation because of not including the heat flow equation.
2) The number of spatial dimensions. For example, including Ohmic conductivity in a 2-D simulation would cover only the center to edge variation across the

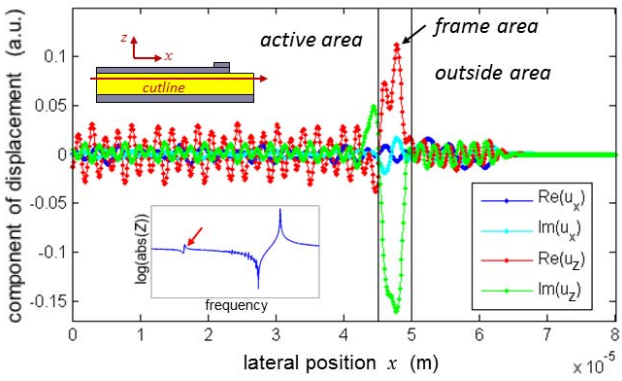

Fig. 20. Cutline of the displacement profile at the frequency of the mode marked by the red arrow in the impedance characteristics (inset, bottom left). The resonator comprises a 5-μm-wide raised frame along its perimeter.

resonator, but not the more important x–y distribution of current density and electric potential affected by the position of the contact leads at the resonator's perimeter.

3) The accuracy of the input data, e.g., the dimensions of the structure including the layer thicknesses as well as the material data. Whereas the material properties corresponding to longitudinal waves are reasonably well known as they can be extracted from the electric response and the resonance frequencies, our information on shear wave parameters is typically much less.

The impact of these errors can be almost any number, also depending on the investigated operating condition.

In summary, provided the numerical implementation is done properly, the principle limitations of the physical model and the input data govern the overall simulation accuracy. As shown previously, in most cases, the attainable performance, i.e., the values for the target figures of merit like Q-values, is less accurately reflected, but the ballparks of where to find the optimum device geometry (e.g., the best frame width) can be predicted reliably.

V. Scope of FEM Simulations

Numerical simulations are typically able to provide results much faster than an experiment including sample manufacturing, preparation, and measurement. Besides, they reveal the distributions of internal quantities at a much finer resolution in space and time as any measurement technique can do. This section discusses some important applications of FEM simulations for both research and product development.

A. Understanding Fundamental Effects

1) Identification of Modes: In addition to the main mode, the electric response of a resonator typically comprises a multitude of extra resonances, for example, the well-known spurious modes caused by laterally standing waves in the active area. Besides, also other modes might exist that arise from local effects in resonator regions other than the active area. FEM is an appropriate tool to analyze the cause of the observed modes, which could give valuable hints on how to suppress them. An example is shown in Fig. 20: the impedance characteristics of a resonator with a raised frame include a pronounced mode at a frequency below f_d of the active area (see Fig. 7 for the definition of f_d). The respective displacement profile (see Fig. 20) illustrates that the acoustic energy is focused on the edge of the resonator, i.e., this mode is caused by a local resonance in the frame.

2) Eigenmode Expansion: Further information on the physics of the resonator is obtained by expanding a given displacement profile to eigenmodes. The simplest example is a Fourier transformation, which essentially constitutes an expansion to traveling waves $\exp(ik_x x)$ with a real wave number k_x. This is the most common technique to get the real part of the dispersion diagram [27], [28]. A method for extracting imaginary k_x-values is proposed in [29]: after measuring the displacement profiles outside the active area, the characteristic lengths have been extracted by fitting an evanescent distribution. These techniques are typically used for evaluating measurement results, but they are as well applicable for analyzing displacement profiles calculated by FEM simulations.

For investigating the general case of an arbitrary superposition of traveling and evanescent contributions, the expansion

$$\boldsymbol{u}(x) = c + \Sigma_{n=1}^{N} \mathbf{A}_n \exp\left(k_n^I x\right) \cos\left(k_n^R x + \phi_n\right) \qquad (7)$$

of the lateral displacement profile is proposed. Here, N is the total number of modes and c denotes a constant offset, while $k_x = k_n^R + ik_n^I$, A_n, and ϕ_n represent the k-value, amplitude, and phase of mode n at the considered frequency, respectively. These $4N+1$ unknowns are determined by fitting the expansion to the given displacement distribution. The constant c corresponds to the uniform excitation ($k_x = 0$) that would be the only contribution in a 1-D Mason model. As it does not satisfy the lateral boundary conditions of a 2-D or 3-D structure, the general solution in this case is a superposition that also comprises modes with a nonzero k_x.

A first example is shown in Fig. 21. The total displacement profile is plotted in the top panel of Fig. 21. It obviously includes two standing waves with different lateral wavelengths and similar amplitudes [Fig. 21 (top)]. Each contribution is displayed in a linear scale and a logarithmic scale in Fig. 21 (bottom). The expansion reveals a third standing wave with a significantly lower amplitude as well as a wave with a complex k_x-value where both the real and the imaginary part do not vanish [Fig. 21 (dark blue line)]. The second example at a different frequency (see Fig. 22) also comprises two standing waves, a complex mode, and an evanescent mode with a pure imaginary k_x-value [Fig. 22 (light blue straight line in the logarithmic view)]. Note that any mode whose imaginary part of the k_x-value is not zero has an amplitude that rapidly decreases with distance from the resonator edge, which can be clearly seen in the linear view. Reference [30] reports on experimental investigation of these modes.

As the k_x-values are part of the fitting parameters for any considered frequency, this technique as well enables one to assemble the dispersion diagram, i.e., the relation of ω and k_x for any mode. Note that it reveals any kind of mode, real, imaginary, or complex. Fig. 23 compares

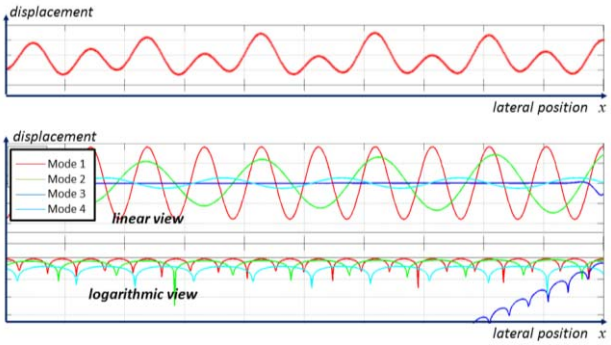

Fig. 21. Top: modal expansion of the displacement profile. Bottom: the contribution of each individual mode is plotted separately in a linear scale and a logarithmic scale.

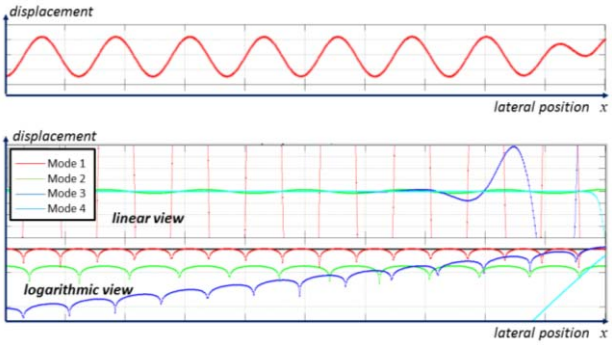

Fig. 22. Top: second example for a modal expansion of the displacement profile. Bottom: the contribution of each individual mode is plotted separately in a linear scale and a logarithmic scale.

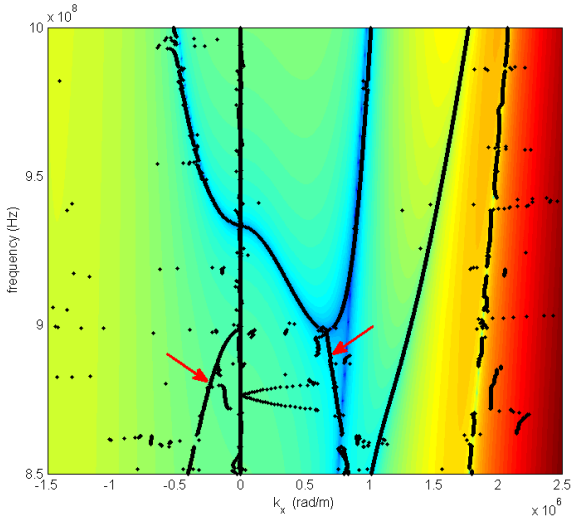

Fig. 23. Comparison of dispersion diagrams. Each black dot represents the k_x-value of a mode that has been found by the modal expansion of (7) at a considered frequency. The real part of k_x is plotted on the positive k_x-axis and the imaginary part in the negative k_x-axis. The two parts marked by the red arrows represent the complex branch below f_d. For reference, the color-shaded plot refers to the dispersion diagram calculated by the commonly used matrix techniques [18]–[20] with propagating modes plotted in the positive k_x-axis and evanescent modes plotted in the negative k_x-axis.

the (k_x, f) combinations obtained by postprocessing FEM results according to (7) with the dispersion diagram calculated by the commonly employed matrix techniques [18]–[20].

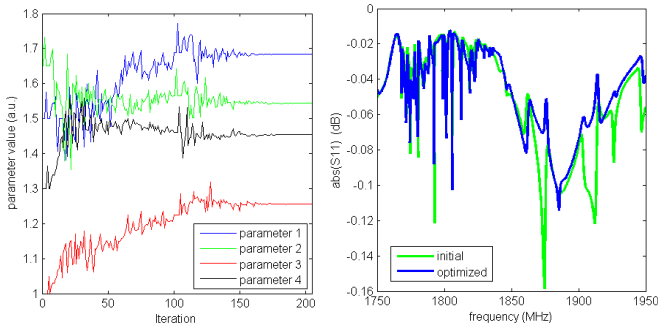

Fig. 24. Optimizing the edge termination by a raised and a recessed frame. Left: the evolution of the parameter values during the iterative optimization. Right: comparison of the resonator response before and after optimization. For a perfect resonator, $S_{11}(f)$ would be equal to 1 at any frequency, which corresponds to the zero line of the logarithmic plot.

While the dispersion branches of some weakly excited modes (e.g., the one at k_x-values around 2 rad/μm) are not very reliably extracted by the expansion of (7), the results for the modes with pronounced amplitude, in particular the main mode, are in excellent agreement with the classical dispersion calculation.

B. Design Support

In the previous section, it has been demonstrated that 2-D FEM simulations can accurately predict the optimum configuration of some important aspects of the BAW resonator design. Since today's computers allow completing a frequency sweep of a 2-D model in a few minutes, FEM is an attractive tool also for designing products. A natural approach is to scan a parameter space, for example, frame widths as shown in Figs. 14–17.

More detailed numbers are obtained by combining the FEM simulator with an optimizer. For that purpose, targets for the figures of merit and a set of parameters, e.g., frame sizes, are selected. Based on the design corresponding to the current values of these parameters, an FEM simulation provides the terminal response. From that, some figures of merit are extracted and passed to the optimizer that calculates the parameter values for the next iteration.

As an example, let us look at the edge termination of a resonator by a recessed and a raised frame, with thicknesses and widths of the two frames being the four design parameters. The optimization target is to maximize $S_{11}(f)$ in the entire frequency interval. The iterative optimizer [31] converges after about 15 h with about 200 iterations (see Fig. 24). Compared with the initial configuration, the S_{11}-parameter of the optimized response is closer to 1 (i.e., the zero line in the logarithmic view); in particular, some spikes down to lower values have been mitigated, which can be a very desired benefit for using the resonator in a filter. Note that the total computation time is governed by the FEM simulation, and hence the best way to speed up the optimization is reducing the number of FEM calls. For that purpose, a different optimization technique and/or a more efficient tool coupling can be helpful. An interesting method is reported in [32]: The right-hand side of the system of equation is modified so that the FEM simulation also returns the Jacobian matrix, i.e., the

derivatives with respect to the optimization parameters, during the same simulation run, and thus less FEM calls are needed for a gradient-based optimization.

It should be mentioned that two preconditions are required to make optimization results useful. First, since any simulation output can be just as good as the input, reliable information on the structure (e.g., layer thicknesses) and on material parameters are needed. In particular, determining material parameters accurately is a major effort. Second, final parameter values are typically rather close to the initial ones in particular for iterative optimization. That means optimization does not teach something new, but provides only the numbers for fine-tuning a solution that we need to know approximately already in advance.

C. Exploring Novel Concepts

For the benefits outlined above, FEM is as well a valuable tool for exploring novel concepts where initially little know-how is available. An example would be the so-called laterally coupled resonator filter (LCRF): the structure resembles a classical BAW resonator, except that the top electrode is patterned to form an interdigital structure with the fingers connected alternately to a first port or to a second port (see Fig. 25). The electric bias applied to one port creates a vertical electric field that excites a bulk wave. Its lateral profile couples to the area of the fingers connected to the other port, thus transmitting energy between the two electric ports. Each acoustic excitation can form two fundamental types: 1) the symmetric mode, where the motion in the area of port 1 is in phase with the motion in the area of port 2, and 2) the antisymmetric mode, where the sections of the two ports are vibrating in opposite phase. Further information can be found in [33]–[36].

For this type of device, the fundamental resonance frequencies depend not only on the layer stack but also on the lateral geometry, i.e., finger width and gap width. They cannot be calculated by 1-D models—2-D is the least complex model we need. Fig. 25 (bottom) sketches a cross section through the interdigital finger structure and highlights the simulation domain, which can be chosen as small by exploiting the planes of symmetry in the center of the fingers. It allows calculating the fundamental modes but does not cover the intermediate modes with a lateral wavelength greater than the finger pitch [35].

The typical spectrum of LCRF devices shows a multitude of modes. For forming a passband, two or more of them would need to be just right apart in frequency. Besides, any other mode that could transmit energy from one port to the other should be as little pronounced as possible; otherwise, out-of-band rejection will be poor. As the resonances are impacted by both the vertical device design (layer stack) and the lateral configuration (finger and gap widths), modeling is a very welcome aid to explore the complexity of the design space.

Interesting information on the physics of these devices is revealed by an overview of the resonance frequencies versus a considered design parameter. It is created by the strategy illustrated in Fig. 26: for any given value of the design

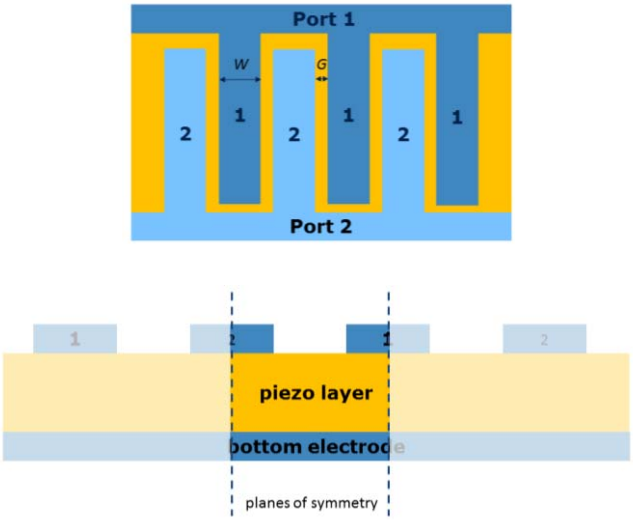

Fig. 25. Geometry of a laterally coupled resonator filter. Top: the top view showing the interdigital structure of the patterned top electrode. Bottom: the layer stack is the same as for classical BAW resonators. Exploiting the symmetry with respect to the center of the fingers allows truncating the simulation domain, as shown in the bottom.

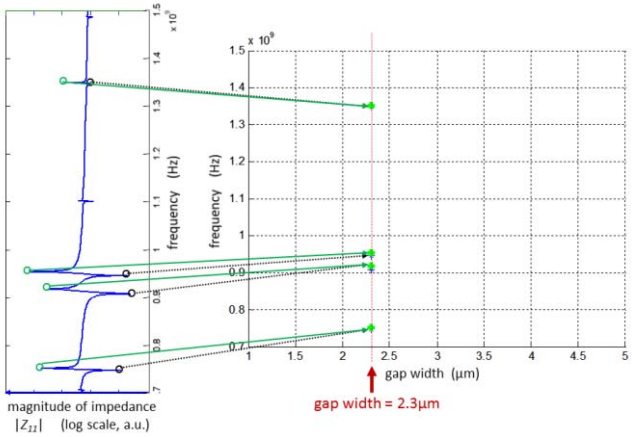

Fig. 26. Left: typical spectrum of an LCRF comprising a multitude of modes. Right: in order to create an overview of modal resonances versus a design parameter (here gap width), the resonances are extracted from the spectrum and marked at the respective value of the design parameter (here gap width is 2.3 μm).

parameter, e.g., a gap width of 2.3 μm, the resonances are extracted from the spectrum and marked in the overview diagram at the respective value of the design parameter. Changing the geometry creates a different spectrum and another set of resonances, finally assembling an overview of how the resonance frequencies are related to the design parameter [Fig. 27 (top)]. For further information, the types of each of the resonances can be identified by snapshots of the displacement profiles. Fig. 27 (bottom) shows examples of the symmetric type and the antisymmetric type of the thickness extensional mode at different geometries. Connecting the markers for the modes of the same type creates branches in the overview diagram, each of which represents a particular kind of resonance.

As an LCRF is a two port device intended to form a filter passband, a similar strategy is used for creating an overview

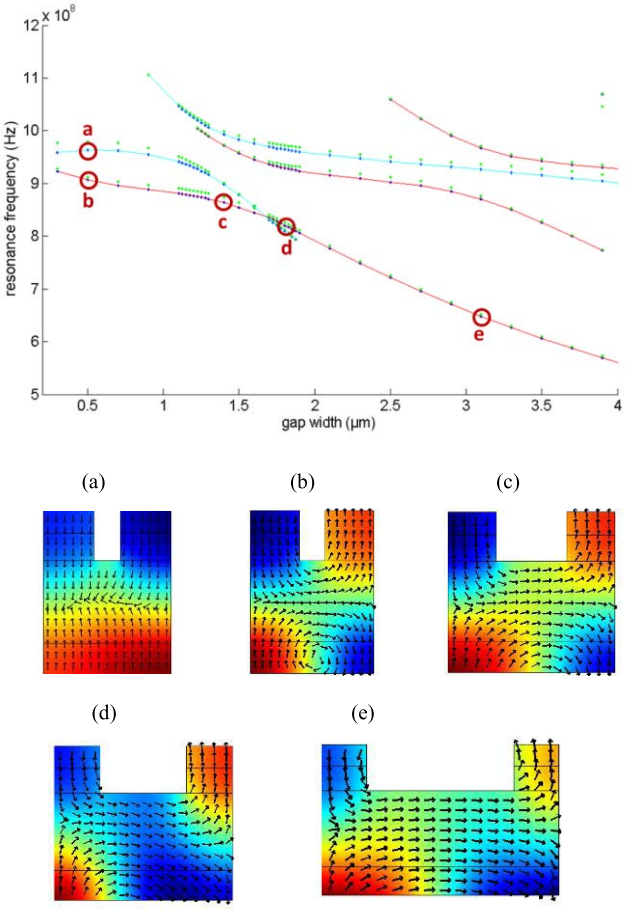

Fig. 27. Top: mode dependence on a design parameter, like gap width. Bottom: the snapshots of the displacement profiles reveal that the mode at the marker labeled (a) is the symmetric type of the thickness extensional mode, while the resonances of the modes labeled (b)–(e) correspond to the antisymmetric type of the TE1 mode. Connecting the markers for resonances of the same type forms branches in the diagram.

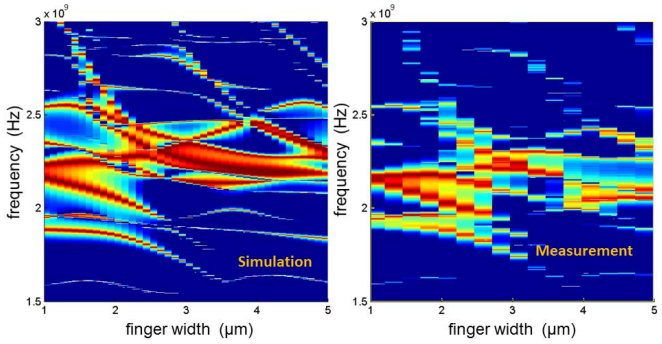

Fig. 28. Insertion loss of an LCRF versus the widths of the fingers in the interdigital structure. The results of a 2-D simulation (left) are compared with the measurement results (right) (red region represents low IL and dark blue region means high IL). The simulation study is based on a much finer step size of the finger width.

of insertions loss versus frequency and a considered design parameter. Again, branches are observed, and it becomes immediately evident at which geometry the modes would be just at the right frequencies for forming the desired passband. Fig. 28 shows an example for different finger widths. The comparison with experimental data confirms that the characteristic features are well predicted by the 2-D FEM simulations, thus demonstrating another example of how FEM can help to explore possible designs of complex resonator devices.

VI. Conclusion

Numerical simulations based on finite-element models become more and more important also for developing BAW technology. We have demonstrated the model setup and implementation; the key aspects are the implementation of proper boundary conditions and a discretization capable of reflecting the physical effects in the resonator. Whereas 3-D simulations are still a considerable effort even with today's computers, many important questions of device physics and design can already be efficiently addressed by 2-D simulations. An important example is edge termination by recessed and raised frames for spurious mode suppression and improving energy confinement. Finite-element models can be flexibly tailored to the specific needs of the desired investigation. In addition to the basic linear electrical and acoustical system, further aspects like the thermal domain or nonlinear effects can be included in the model, which we envision to become major trends in the near future. Thus, finite-element techniques constitute valuable tools for improving our understanding of fundamental effects in the devices like the modal nature, for supporting product design by providing quantitative information on optimum design geometry, and for exploring novel device concepts and pioneering the way into new technologies.

Acknowledgment

The authors would like to thank Avago's experts on FEM and acoustics, R. Ruby, A. Shirakawa, D. Burak, J. Kaitila, and P. Bradley, for their valuable discussions and input.

References

[1] K.-Y. Hashimoto, *RF Bulk Acoustic Wave Filters for Communications*. Norwood, MA, USA: Artech House, 2009.
[2] R. Thalhammer and J. D. Larson, "Finite element analysis of BAW devices: Principles and perspectives," in *Proc. IEEE Ultrason. Symp.*, Oct. 2015, pp. 1–10.
[3] B. A. Auld, *Acoustic Fields and Waves in Solids*. Melbourne, FL, USA: Krieger, 1990.
[4] R. Lerch, "Simulation of piezoelectric devices by two- and three-dimensional finite elements," *IEEE Trans. Ultrason., Ferroelectr., Freq. Control*, vol. 37, no. 2, pp. 233–247, May 1990.
[5] O. Mayer, S. Zaglmayr, K. Wagner, and J. Schöberl, "Perfectly matched layer finite element simulation of parasitic acoustic wave radiation in microacoustic devices," in *Proc. IEEE Ultrason. Symp.*, Oct. 2007, pp. 702–706.
[6] J.-P. Berenger, "A perfectly matched layer for the absorption of electromagnetic waves," *J. Comput. Phys.*, vol. 114, no. 2, pp. 185–200, Oct. 1994.
[7] W. C. Chew and Q. H. Liu, "Perfectly matched layers for elastodynamics: A new absorbing boundary condition," *J. Comput. Acoust.*, vol. 4, no. 4, pp. 341–359, 1996.
[8] F. D. Hastings, J. B. Schneider, and S. L. Broschat, "Application of the perfectly matched layer (PML) absorbing boundary condition to elastic wave propagation," *J. Acoust. Soc. Amer.*, vol. 100, no. 5, pp. 3061–3069, 1996.
[9] M. Kaltenbacher and R. Lerch, "Perfectly matched layer technique for the numerical computation of wave propagation phenomena," in *Proc. IEEE Ultrason. Symp.*, Oct. 2007, pp. 183–186.

[10] K. Tajic, A. Volatier, R. Aigner, and M. Solal, "Simulation of solidly mounted BAW resonators using FEM combined with BEM and/or PML," in *Proc. IEEE Ultrason. Symp.*, Oct. 2010, pp. 181–184.
[11] A. Shaposhnikov, M. Kaltenbacher, and P. Nicolay, "Fast full-FEM computation of COM parameters. Application to multilayered SAW structures," in *Proc. IEEE Ultrason. Symp.*, Sep. 2014, pp. 1501–1504.
[12] R. Lerch, M. Kaltenbacher, H. Landes, and P.-C. Eccardt, "Combination of finite element and boundary element methods in computational acoustics and coupled-field problems of electro-acoustic transducers," in *Boundary Elements in Acoustics*, O. von Estorff, Ed. Ashurst Lodge, U.K.: WIT-Press, 2000.
[13] V. Laude, C. Jerez-Hanckes, and S. Ballandras, "3D piezoelectric surface Green's function," in *Proc. IEEE Ultrason. Symp.*, Sep. 2005, pp. 687–690.
[14] D. Ekeom, B. Dubus, and A. Volatier, "Solidly mounted resonator (SMR) FEM-BEM simulation," in *Proc. IEEE Ultrason. Symp.*, Oct. 2006, pp. 1474–1477.
[15] D. Ekeom and B. Dubus, "Thermoelastic FEM-BEM model for solidly mounted resonator," in *Proc. IEEE Ultrason. Symp.*, Nov. 2008, pp. 1564–1567.
[16] R. Thalhammer and R. Aigner, "Energy loss mechanisms in SMR-type BAW devices," in *Proc. IEEE MTT-S Microw. Symp.*, Jun. 2005, pp. 1–4.
[17] R. Thalhammer, G. Fattinger, M. Handtmann, and S. Marksteiner, "Ohmic effects in BAW-resonators," in *Proc. IEEE MTT-S Microw. Symp.*, Jun. 2006, pp. 390–393.
[18] E. L. Adler, "Matrix methods applied to acoustic waves in multilayers," *IEEE Trans. Ultrason., Ferroelectr., Freq. Control*, vol. 37, no. 6, pp. 485–490, Nov. 1990.
[19] A. Reinhardt, T. Pastureaud, S. Ballandras, and V. Laude, "Scattering matrix method for modeling acoustic waves in piezoelectric, fluid, and metallic multilayers," *J. Appl. Phys.*, vol. 94, no. 10, pp. 6923–6931, Nov. 2003.
[20] T. Pastureaud, V. Laude, and S. Ballandras, "Stable scattering-matrix method for surface acoustic waves in piezoelectric multilayers," *Appl. Phys. Lett.*, vol. 80, no. 14, pp. 2544–2546, Apr. 2002.
[21] *PARDISO Project*, accessed 2016. [Online]. Available: http://ww.pardiso-project.org
[22] *MUMPS*, accessed 2016. [Online]. Available: http://mumps.enseeiht.fr
[23] J. Kaitila, M. Ylilammi, J. Ella, and R. Aigner, "Spurious resonance free bulk acoustic wave resonators," in *Proc. IEEE Ultrason. Symp.*, Oct. 2003, pp. 84–87.
[24] R. C. Ruby, "FBAR technology," in *RF Bulk Acoustic Wave Filters for Communications*, K.-Y. Hashimoto, Ed. Norwood, MA, USA: Artech House, 2009.
[25] R. Thalhammer, J. Kaitila, R. Aigner, and S. Marksteiner, "Prediction of BAW resonator performance using experimental and numerical methods," in *Proc. IEEE Ultrason. Symp.*, Aug. 2004, pp. 282–285.
[26] R. C. Ruby, P. Bradley, Y. Oshmyansky, A. Chien, and J. D. Larson, "Thin film bulk wave acoustic resonators (FBAR) for wireless applications," in *Proc. IEEE Ultrason. Symp.*, Oct. 2001, pp. 813–821.
[27] P. T. Tikka *et al.*, "Laser probing and FEM modeling of solidly mounted resonators," in *Proc. IEEE MTT-S Microw. Symp.*, Jun. 1999, pp. 1373–1376.
[28] K. L. Telschow and J. D. Larson, III, "Quantitative determination of lateral mode dispersion in film bulk acoustic resonators through laser acoustic imaging," in *Proc. IEEE Ultrason. Symp.*, Oct. 2006, pp. 448–451.
[29] K. Kokkonen, J. Meltaus, T. Pensala, and M. Kaivola, "Measurement of evanescent wave properties of a bulk acoustic wave resonator [Letters]," *IEEE Trans. Ultrason., Ferroelectr., Freq. Control*, vol. 59, no. 3, pp. 557–559, Mar. 2012.
[30] J. Kaitila and J. D. Larson, "Complex peripheral Lamb modes in FBARs," in *Proc. IEEE Ultrason. Symp.*, Jul. 2013, pp. 757–760.
[31] J. C. Lagarias, J. A. Reeds, M. H. Wright, and P. E. Wright, "Convergence properties of the Nelder–Mead simplex method in low dimensions," *SIAM J. Optim.*, vol. 9, no. 1, pp. 112–147, 1998.
[32] F. Vogel, H. Landes, R. Lerch, M. Kaltenbacher, and R. Peipp, "Numerical simulation and optimization of capacitive transducers," in *Proc. Int. Conf. EuroSimE*, 2003, pp. 1–7.
[33] J. Meltaus, T. Pensala, K. Kokkonen, and A. Jansman, "Laterally coupled solidly mounted BAW resonators at 1.9 GHz," in *Proc. IEEE Ultrason. Symp.*, Sep. 2009, pp. 847–850.
[34] T. Pensala, J. Meltaus, and M. Ylilammi, "An eigenmode superposition model for lateral acoustic coupling between thin film BAW resonators," in *Proc. IEEE Ultrason. Symp.*, Nov. 2008, pp. 1540–1543.
[35] J. Meltaus, T. Pensala, and K. Kokkonen, "Parametric study of laterally acoustically coupled bulk acoustic wave filters," *IEEE Trans. Ultrason., Ferroelectr., Freq. Control*, vol. 59, no. 12, pp. 2742–2751, Dec. 2012.
[36] K. Wang, U. Koelle, J. D. Larson, R. Thalhammer, and S. Martin, "FBAR laterally coupled resonator filter," in *Proc. IEEE Ultrason. Symp.*, Oct. 2015, pp. 1–5.

Robert K. Thalhammer (M'16) received the M.Sc. and Ph.D. degrees in physics from the Munich University of Technology, Munich, Germany, in 1994 and 2000, respectively. His studies were focused on solid-state physics, in particular, the self-consistent modeling of vertical cavity surface emitting lasers.

From 1994 to 2000, he was a Research Scientist with the Munich University of Technology, where he was involved in consistent modeling and simulation of electric, thermal, and optical interacting systems. In 2000, he joined Infineon Technologies, Munich. Since 2003, he has been involved in bulk-acoustic-wave technology, including finite-element modeling for the electric and acoustic simulation of resonators. He is with Avago Technologies (now Broadcom Ltd) since 2008, where his major focuses are film bulk acoustical resonators physics, multiphysics modeling, and novel bulk-acoustic-wave (BAW) device concepts. He has authored or coauthored many journal articles, conference publications, and patents. His current research interests include design, modeling, simulation, and characterization of discrete RF structures, such as RF transistors and RF microelectromechanical systems.

Dr. Thalhammer serves on the International Ultrasonics Symposium (IUS) Technical Program Committee.

John D. Larson, III (S'61–M'63–SM'80–LF'06) was born in Klamath Falls, OR, USA. He received the S.B.E.E. degree in electrical engineering from the Massachusetts Institute of Technology, Cambridge, MA, USA, in 1962, and the Ph.D. degree in electrical engineering from Stanford University, Stanford, CA, USA, in 1971, with a thesis on creating, analyzing, and modeling thin piezoelectric films for use at microwave frequencies.

He took a five-year industrial education stint with the Instrument Division, Varian Associates, Palo Alto, CA, USA. He joined Hewlett-Packard (H-P) Laboratories, Palo Alto, in 1972, as a member of the Technical Staff, where he was involved in laser acoustics, surface acoustical wave devices, and spectrophotometry, and then moving into cardiac acoustical imaging, resulting in a major new business for H-P. He moved into cardiac magnetic resonance imaging, and recently switched completely to film bulk acoustical resonators (FBAR). This latter work was continued at spin-off companies, such as Agilent Technologies, Avago Technologies, and most recently Broadcom Technologies, San Jose, CA, USA. It has resulted in the major application of FBAR technology to cellular handheld communication devices and nucleated a very large contribution to cellular handheld communication devices. He is currently a Distinguished Scientist with Broadcom Ltd. He has authored many articles, conference proceedings, and patents relating to these fields.

Dr. Larson is a Life Fellow of the S-UFFC Society. He has served the S-UFFC in many capacities, helping to lead IUS meetings, serving on the AdCom Committee, and providing technical leadership in the Physical Acoustics Group of S-UFFC.